New Journal of Physics
The open access journal at the forefront of physics

Deutsche Physikalische Gesellschaft DPG
IOP Institute of Physics

Published in partnership with: Deutsche Physikalische Gesellschaft and the Institute of Physics

OPEN ACCESS

RECEIVED
25 December 2015

REVISED
28 February 2016

ACCEPTED FOR PUBLICATION
30 March 2016

PUBLISHED
13 April 2016

PAPER

Surface plasmon polariton modes in coaxial metal-dielectric-metal waveguides

Marie Anne van de Haar, Ruben Maas, Benjamin Brenny and Albert Polman

Center for Nanophotonics, FOM Institute AMOLF, Science Park 104, 1098 XG, Amsterdam, The Netherlands

E-mail: polman@amolf.nl

Keywords: metamaterials, plasmonics, cathodoluminescence spectroscopy, waveguides

Abstract

We explore the optical properties of a coaxial plasmonic metamaterial consisting of hollow dielectric cylinders with a diameter of 100–250 nm and a ring wall width of 10–50 nm, embedded in metal. We investigate the modal electric and magnetic fields and dispersion relation for different geometries and material choices of a single coaxial channel by using realistic values for all design parameters. The Fabry–Pérot modes of a finite thickness slab are investigated with cathodoluminescence spectroscopy and explained by extracting the mode index from FDTD simulations. Furthermore, we investigate the coupling behavior of adjacent coaxes inside a hexagonal array. We find a change from the single-ring dispersion relation for coaxes with a ring-to-ring distance smaller than 20 nm.

1. Introduction

The refractive index n of a material determines how an electromagnetic wave interacts with the material. Conventional media always slow down the light, and consequently shrink the wavelength, with a factor determined by the refractive index. In the field of metamaterials, where materials are designed by using sub-wavelength building blocks, materials can be realized with effective optical properties beyond what is possible with natural materials. One important class of optical metamaterials is composed of noble-metal resonant structures with a magneto-electric response (e.g. split-ring resonators), embedded in a dielectric material. The interplay between the magnetic and electric resonances can lead to an effective refractive index that is negative [1], which implies that the phase velocity of light is negative and light shows negative refraction at an interface [2–4]. However, using small resonant building blocks has several major limitations. These designs suffer from high Ohmic dissipation losses [5] and work for a limited bandwidth. Furthermore, in order for them to operate in the visible spectral range, the structures must be scaled down [6] to length scales where fabrication is hardly possible using currently available nano-fabrication techniques.

An alternative way to modify the wavelength of a traveling electromagnetic wave is to couple the light into a bound mode on a metal-dielectric interface. The mode index of such a traveling surface plasmon polariton (SPP) can have a value much larger than found in naturally homogeneous materials, enabling high confinement and hence a very high local field intensity [7–15]. Proper design of (coupled) plasmonic waveguides can even result in extreme cases, for instance a negative index of refraction [16–20] or an index near zero [21–23]. This would enable new applications such as a flat lens [24–26] which would enable for example new recording devices, novel (micro-)optical components [27, 35, 47] for optoelectronic integration, superradiant light sources which can be used to realize low-power LED and laser devices, and transformation optics [28] and optical cloaking [29–33] leading to for example enhanced absorption in photovoltaic devices.

Earlier work on (coaxial) plasmonic metamaterials [20, 36, 37] theoretically describe the behavior of these kind of materials. However, a full theoretical model describing the full optical properties of the metamaterial including the incoupling from free-space radiation, reflection and phase-shifts on both metamaterial surfaces and the modal behavior inside the waveguide channels as proven to be extremely difficult, if not impossible to realize. The incoupling, for example, is very difficult to describe due to the many modes that contribute and influence the incoupling efficiency of the fundamental mode by changing the near-field near the metamaterial

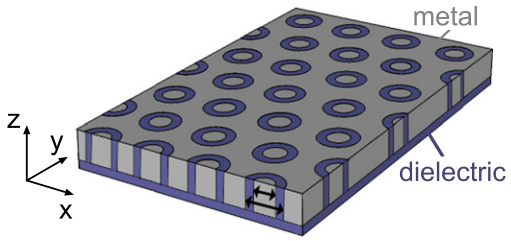

Figure 1. Sketch of the coaxial plasmonic metamaterial. The coaxial waveguides consist of thin (10–30 nm) dielectric channels (purple) having an outer diameter of 00–200 nm embedded in metal (gray) and supported by a dielectric bulk material.

surface. Instead, we show in the paper that a theoretical model that solves Maxwells equations in cylindrical coordinates can be used to approximate the behavior in finite-size coaxes in an array. The index that is deduced from this method contains all information of the propagation inside the channels. In the paper we show that this single-coax approximation breaks down for channel-to-channel distances smaller than 50 nm.

Using this coupled SPP principle, a coaxial design was proposed where the double periodically stacked MDM SPP waveguides are wrapped into a coaxial geometry [36, 37, 48], resulting in a polarization independent metamaterial. A sketch of the design is shown in figure 1, where the coaxial waveguides are placed in a hexagonal array. This design has been shown to exhibit a negative mode index for visible wavelengths [48]. Here, we explore the optical properties of this coaxial plasmonic metamaterial in more detail. We show the trends in wavelength for different material and geometry choices, using realistic values for all design parameters. Furthermore, we investigate the coupling behavior between adjacent coaxial channels, which gives an extra degree of freedom to tune the SPP mode profiles. Our theoretical and numerical work is supported by high resolution cathodoluminescence (CL) measurements on experimentally fabricated coaxial waveguides.

2. Waveguide dispersion inside plasmonic coaxial channels

The mode dispersion of coupled SPP waveguides is the result of a complex field overlap between the different SPPs on each interface, where only small changes in the coax geometry or used material properties can significantly change this overlap, and subsequently the modal dispersion. Therefore it is difficult to intuitively predict the dispersion behavior of the modes present in the coaxial waveguides. Instead, we explore some general trends for using different materials and coax geometries by calculating the mode dispersion diagrams of single plasmonic coaxial waveguides with different geometries and material choices. For this we use the method described in [36, 37], where Maxwell's equations are solved in cylindrical coordinates for a single infinitely long coax embedded in an infinitely large metal slab. Only the first azimuthal mode number is considered, since these are the lowest order modes that can couple to free space radiation.

Figure 2 shows a cross section and top view of the H_y fields (where the coordinates are defined as in figure 1) of the two modes which have the lowest loss, in a single coax (with azimuthal mode order 1). These are the two modes we will consider in the rest of this paper. Figures 2(a) and (b) shows a symmetric mode, where the H_y field does not change sign across the dielectric channel. The mode shown in figures 2(c) and (d), represents the field of an anti-symmetric mode, of which the H_y field does change sign across the waveguide. If we consider the time dependence of both fields, we find that the symmetric mode is characterized by a positive phase velocity, and thus a positive mode index, and the antisymmetric mode shows a negative phase velocity, which is characteristic for a negative mode index.

2.1. Dielectric material and metal choice

Next, we explore how the dispersion behavior of the two modes shown in figure 2 depends on the used metallic and dielectric materials. Figure 3 shows the dispersion of an infinitely long, 20 nm wide coaxial channel of vacuum ($n = 1$), SiO_2 ($\mathrm{Re}(n) \sim 1.5$) and Si ($\mathrm{Re}(n) \sim 3.5$–6.5) embedded in either silver or gold. For the calculations we used the complex optical constants as determined by Palik [38] and Johnson and Christy [39] for the dielectric and metal, respectively. Both the real and the imaginary part of the wave vectors in the direction of traveling (z) are plotted, where the absolute value of the real part determines the SPP wavelength and the imaginary part represents the losses from which the propagation length $L_{\mathrm{SPP}} = 1/(2\ \mathrm{Im}\ (k_z))$ can be easily calculated. In order to have a negative index, the direction of the Poynting vector $\mathbf{S}$ must be opposite to the wave vector $\mathbf{k}$ ($\mathbf{k} \cdot \mathbf{S} < 0$) [20, 40, 41]. Since we only consider modes with a positive energy velocity, which corresponds to a positive imaginary part of the wave vector, the positive or negative nature of the mode is

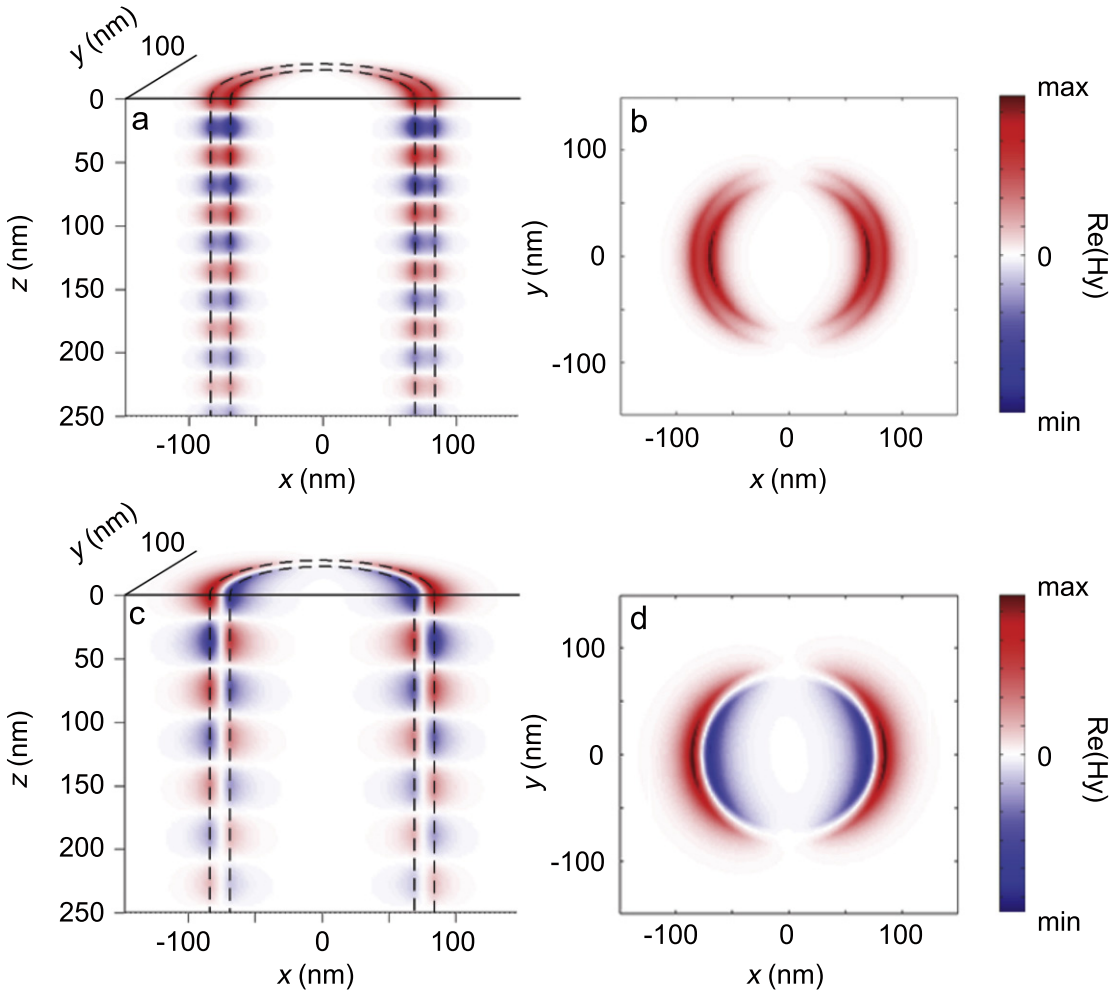

Figure 2. Plots of the H_y fields of the two modes with the lowest losses inside an infinitely long, single Si coax channel embedded in Ag, having an outer diameter of 150 nm and a channel thickness of 20 nm. (a) Cross section through the *xz* and (b) *xy* plane of the H_y fields of the symmetric and (c) and (d) the anti-symmetric coupled SPP mode. The dashed lines represent the contours of the coaxial channels. Both modes are calculated at a wavelength where the depicted mode is dominant, (a) and (b) at a wavelength of $\lambda = 673$ nm and (c) and (d) at $\lambda = 524$ nm.

determined by the sign of the real part of the wave vector. In the rest of this paper we use the term 'negative index mode' for the lowest loss mode which is described by a negative mode index in a part of the investigated frequency regime. The negative index regime of this mode is characterized by a negative propagation of the phase fronts and an asymmetric mode profile of the H_y fields.

Figure 3 shows the existence of both a positive and negative index mode in the UV/visible regime for all material combinations explored in the figure. However, not all material combinations show a dominant region of the negative index mode in the considered wavelength regime, where the dominant mode is defined as the mode with the lowest imaginary part of k_z. From (a) we notice that the material choice of both the dielectric and the metal determine the spectral position and the magnitude of the maximum absolute value of k_z. The frequency at which k_z has its maximum is defined as the SP resonance frequency (ω_{SP}). For a single metal/dielectric interface, the SP resonance frequency is proportional to the plasma frequency (ω_P) of the metal and the dielectric permittivity of the dielectric material via

$$\omega_{sp} \sim \frac{\omega_p}{\sqrt{1+\epsilon_d}}. \quad (1)$$

Considering the different dielectrics, the waveguides built from the high index material Si show the highest confinement, lowest losses and largest negative index frequency region of the considered materials, which is in agreement with [36]. Furthermore, we find that, in accordance with equation (1), the dielectrics with the smallest real values of their refractive indices have their SP resonance at higher frequencies. Interestingly, if we consider the losses of the different waveguide materials we conclude that for the positive-index mode SiO_2 has the lowest losses, while for the negative-index modes Si, of which the refractive index intrinsically has the highest losses,

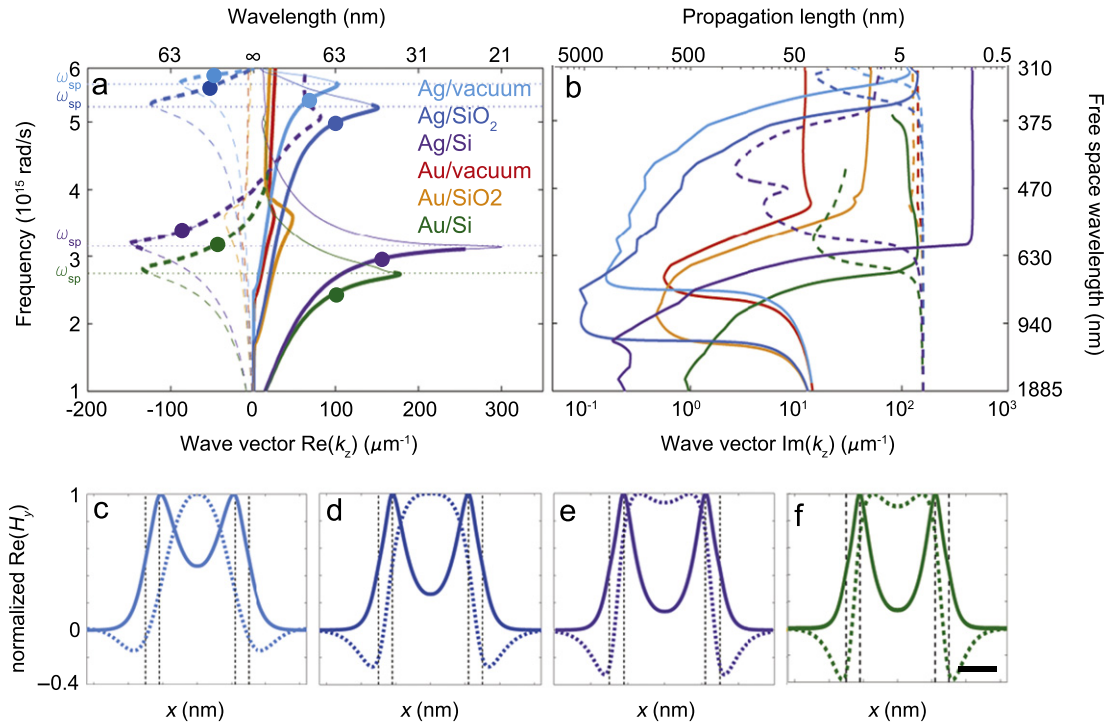

Figure 3. Mode dispersion diagrams of coaxial waveguide channels in the visible spectral range. The outer coax diameter is 150 nm with a 20 nm wide dielectric channel. The dispersion is calculated for three different dielectric materials (air, SiO_2 and Si) and two different metals (Ag and Au) for SPPs traveling in the positive z-direction. Both the real (a) and imaginary (b) part of the wave vector k_z are shown. The negative index modes are indicated with a dotted line, the positive index modes with a solid line. The regions in which the modes are dominant (determined by the lowest losses) are represented as bold lines. (c)–(f) Show the real part of the normalized H_y fields on a cross section through the center of the cylinders. Again, the solid lines represent the positive index mode and the dashed lines the negative index mode. The frequency of the plotted figures is represented by the dot in figure (a). The scale bar represents 50 nm.

results in the lowest SPP losses. This indicates that in the case of SiO_2 the field profile of the negative-index mode is relatively more localized inside the metal, which results in increased dissipation losses.

For the metals we find similar trends for the SP resonance frequencies as for the dielectrics, where the geometries with the plasma frequency at the shortest wavelength, Ag, result in the most blue shifted SP resonances. The absolute value of $\mathrm{Re}(k_z)$ at the SP resonance frequency, however, is larger for the lowest permittivity metal Ag. If we consider the losses we find lower losses for the Ag containing structures, in line with the lower losses of bulk Ag compared to Au in the considered spectral regime.

Figures 3(c)–(f) shows the H_y fields on a cross section through the center of the cylinders. We find that for all positive modes (solid lines) the H_y field does not change sign, and the overall mode profile across the channels is symmetric. The negative index mode changes sign across the waveguide channel, but shows an overall symmetric profile over both waveguide channels. The sign change across the dielectric channel results in a relatively large part of the field being localized inside the metal. As a result, this mode can have a negative mode index, where both the phase fronts propagate backwards and refraction is negative.

In the rest of this paper, we will consider Ag/Si coaxes because of their large negative index frequency region, the possibility to obtain the most extreme mode index and the relatively low losses. However, depending on the applications of interest, in other parts of this thesis we occasionally use Au/Si or Au/SiO_2 for practical reasons.

2.2. Tuning the cylinder outer diameter

Next, we investigate the influence of changing the diameter and channel width of the coaxial waveguide channels. Figure 4 shows the dispersion diagrams of Si/Ag coaxes with a fixed channel width of 20 nm and a varying outer diameter. Firstly we notice that all considered geometries show strong confinement around the SP resonance frequency, with values above 400 μm^{-1} for the real part of k_z. However, for the geometry in this figure, an increase of the absolute value of k_z always results in increased losses as well. The SP resonance is at the same wavelength for all considered geometries, since it is determined by the optical constants of the materials (equation (1)) rather than by the geometry. Interestingly, the waveguides all show a negative-index mode which is dominant for wavelengths shorter than ~630 nm. We note, however, that there exists a third, positive-index

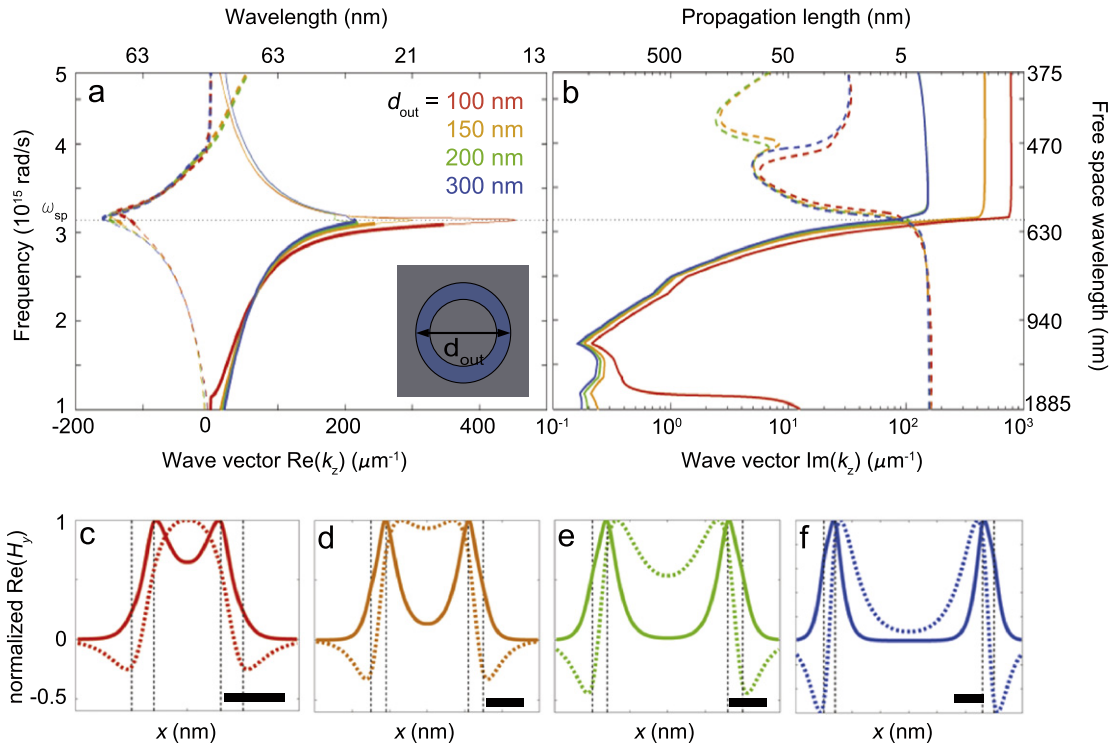

Figure 4. (a) Real and (b) imaginary part of the dispersion diagrams of Ag/Si coaxial waveguides with a 20 nm wide channel and varying diameter. The negative-index modes are indicated with a dashed line, the positive-index modes with a solid line. The dominant regions of the modes are emphasized with a bold line. In case of the smallest and largest outer diameters there is another, positive index, dominant mode above 4×10^{15} rad s^{-1} (not shown here). (c)–(f) Show the H_y field profiles for the different coax geometries, where again the positive-index mode is represented by the solid line and the negative-index mode with a dashed line. The positive-index mode was plotted at $\lambda = 673$ nm, the negative-index mode at $\lambda = 524$ nm. The colors correspond to the same material combinations as indicated in (a). The scale bars in (c)–(f) represent 50 nm.

mode which is dominant above 4×10^{15} rad s^{-1} (corresponding to wavelengths smaller than $\lambda = 470$ nm) in case of the 100 and 300 nm diameter coaxes (not shown here).

Considering the positive-index waveguide modes in figure 4(a), we observe an increase of Re(k_z) at frequencies near the SP resonance frequency, which is most pronounced for the coax with the smallest diameter. The change in k_z is due to a different mode coupling through the metal cladding, as seen from the H_y field plots in figures 4(c)–(f). For the largest two considered diameters, the H_y field goes to zero in the center for the positive index mode, resulting in an almost unaffected relative field distribution inside the dielectric channels, and very similar dispersion behavior of these two modes. For smaller diameters, however, the fields on both sides of the channels do overlap in the coax core, giving rise to a change in the dispersion. The negative-index mode on the contrary, does show non-zero field intensity in the center region of the metal for all diameters. The relative field distributions inside the dielectric channels however, are almost unaffected which results in an almost equal k_z for the negative-index mode for all shown diameters.

The losses show small variations for the different investigated diameters. In general the losses of the positive mode index are slightly larger for smaller diameters. In case of the negative mode index all shown coax dimensions show similar losses up to ~470 nm. For shorter wavelengths, however, the modes inside the largest and smallest diameter coaxes show significantly higher losses than the 150 and 200 nm diameter coaxes.

We conclude that within the outer diameter range of 150–200 nm, while keeping the channel width and materials unchanged, the waveguide modes in the plasmonic coaxes are very similar over the investigated wavelength range. Within this range both the trends and the absolute values of the real and imaginary parts of the wave vectors are the same within a few percent. Although a smaller diameter, of 100 nm, does result in a more extreme mode index near the SP resonance frequency, this geometry shows higher losses and a smaller wavelength range for which the negative index mode is negative. Therefore we study the 150–200 nm diameter coaxes in the remainder of this paper.

2.3. Tuning the dielectric waveguide width

Lastly, we explore the influence of the channel width on the dispersion of the coaxial waveguides, as shown in figures 5(a) and (b). We observe a large difference in both the real and the imaginary parts of the wavevector for

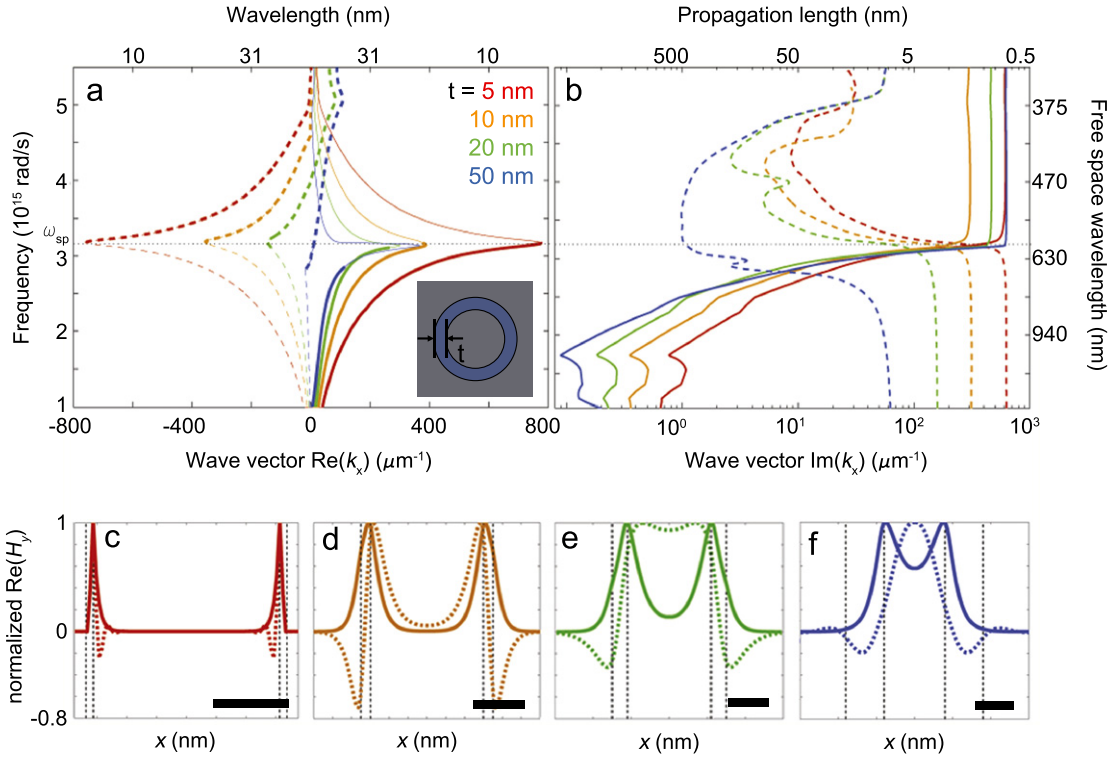

Figure 5. (a) Real and (b) imaginary part of the dispersion diagrams of Si/Ag coaxial waveguides with an average diameter of $r_{out} - r_{in} = 130$ nm and varying channel width. The negative-index modes are indicated with a dashed line, the positive-index modes with a solid line. The dominant regions of the modes are emphasized with a bold line. In case of the smallest and largest outer diameters there is a second positive dominant mode above 4×10^{15} rad s^{-1}. (c)–(f) Shows the H_y field profile for the different channel geometries, where again the positive-mode is represented by the solid line and the negative-mode with a dashed line. The positive-mode was plotted at $\lambda = 673$ nm, the negative-mode at $\lambda = 524$ nm. The scale bars in (c)–(f) represent 50 nm.

changing channel widths in the range 5–50 nm. Using very thin channels on the order of <10 nm, extremely high absolute values of both the positive and the negative mode indices can be obtained. However, as for the other considered SPP designs, increasing the absolute value of the mode index goes together with a decreased propagation length.

In order to understand the trends observed in figures 5(a) and (b), we consider the H_y fields on a cross section of the waveguide channels in figures 5(c)–(f). We observe that the field profile inside the metal, indicating the coupling between the SPPs in both dielectric channels, changes for different channel thicknesses. Furthermore, the field profiles inside the channels also change for different channel thicknesses. For small channel thicknesses, relatively more field is confined inside the metal. This enhanced interaction with the negative permittivity of the metal explains the more negative values of the mode index for smaller waveguide thicknesses. Furthermore, the increase in losses for thinner coax channels is also due to increased dissipation losses as result of the field localization in the metal.

In conclusion, an optimum geometry to obtain coaxial waveguides with a clear negative mode index and relatively low losses, has a channel width of 10–30 nm and an outer diameter of 150–200 nm.

In the previous sections we investigated the optical response of the plasmonic cylindrical metamaterial by considering a single, infinitely long coax. In the next sections, we will consider a hexagonal array of coaxes. We investigate if a single, infinitely long coax is indeed a valid approximation for a finite-thickness hexagonal array of coaxes, both experimentally using CL imaging spectroscopy, and numerically using finite-difference time-domain (FDTD) simulations.

3. CL spectroscopy on a plasmonic coaxial metamaterial

In this section we perform CL spectroscopy measurements on a hexagonal array of coaxial waveguides. From the measured spectra we deduce the mode indices by matching the peaks in measured intensity to Fabry–Pérot oscillations inside the metamaterial slab.

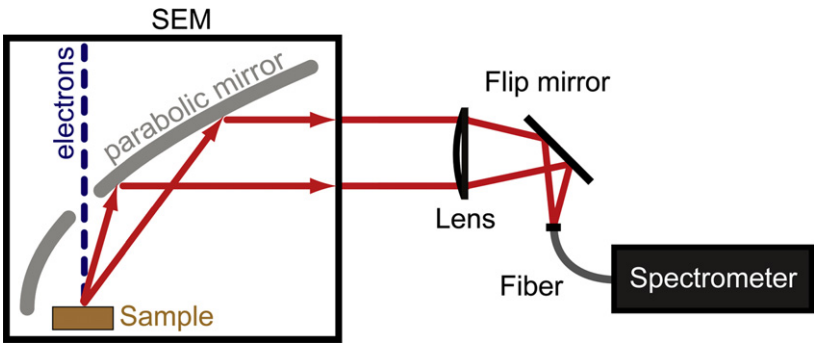

Figure 6. Sketch of the setup used for the CL measurements. The sample is excited using a 30 keV electron beam inside a conventional SEM. The emitted light is collected by a parabolic mirror placed between the sample and the electron column and focused to an optical fiber which guides the signal to a spectrometer.

3.1. CL spectroscopy method

In CL spectroscopy an electron beam of a scanning electron microscope (SEM) is used to locally excite the sample with very high spatial resolution. The electric field generated by the electron beam coherently excites resonant modes supported by the coaxial waveguides with an excitation efficiency dependent on the out-of-plane component of the local density of optical states [42, 43]. The light emitted from excited modes radiating into the far field is collected by an Al parabolic mirror placed between the sample and the electron column and is directed onto a spectrometer. A sketch of the setup is shown in figure 6.

We laterally raster scan the electron beam in steps of 5 nm over a single coax and collect the spectrum for each excitation position. At the same time the secondary electron signal is collected, such that we can match the obtained radiation spectrum with the excitation position on the sample. After correcting for the system response we spatially average the spectrum over all positions of a single ring (including the center area) and normalize to its maximum intensity.

3.2. Sample fabrication

The sample fabrication process for the CL experiment was started with writing rings with a 30 keV electron beam into the negative high resolution resist hydrogen silsesquioxane (HSQ) on a Si substrate. The HSQ is developed by two 30 s dips into a 25% solution of tetramethyl ammonium hydroxide (TMAH) solution in water at 50 °C. Then, the hollow cylinders are transferred into the substrate using an HBr reactive ion etch (RIE). After etching the sample was dipped in a 1% HF solution for 10 min to remove the resist remainders. Next, the metal was evaporated using a technique where the excess of metal was shaved off using an argon ion beam after every 10–15 nm of metal deposition. Lastly, the sample surface was polished and the rings were made optically accessible using focused ion beam (FIB) milling under grazing angles. Figure 7(a) shows an SEM image of the sample fabricated for the CL experiment, where the inset shows a cross section of the measured sample. The rings have an outer diameter of 175 nm and a dielectric channel width of 30 nm, which is in the optimum range for having a negative-index mode as defined in section 2. The pitch, defined as the center-to-center distance, is 230 nm.

3.3. CL spectroscopy results

Figure 7(b) shows the normalized measured CL spectrum averaged over a single coax of the array shown in (a). We observe a clear, large peak at a wavelength of $\lambda = 856$ nm, and several smaller peaks which overlap in the wavelength region of 400–700 nm, with peak values at $\lambda = 461,\ 541$ and 603 nm. At $\lambda = 706$ nm there is a dip in the spectrum.

The large peak at $\lambda = 856$ nm in the CL spectrum shown in figure 7 can be understood by considering the finite thickness of the metamaterial, giving rise to Fabry–Pérot oscillations inside the metamaterial slab. Therefore, cross sections were made at different positions on the $20 \times 20\ \mu m^2$ metamaterial field. We found a thickness in the range of 73–140 nm, where the gradient in slab thickness originates from the FIB polishing step in the fabrication process, since the sample is milled under grazing angles. Since this uncertainty in thickness is too large to determine the wavelength of the expected Fabry–Pérot resonances based on the dispersion diagram (figure 8), we simulated the transmission and reflection spectra for a range of thicknesses (70–150 nm) using Lumerical[1]. For the simulations a plane wave is used to excite the metamaterial sample under normal incidence.

[1] Lumerical solutions, inc.

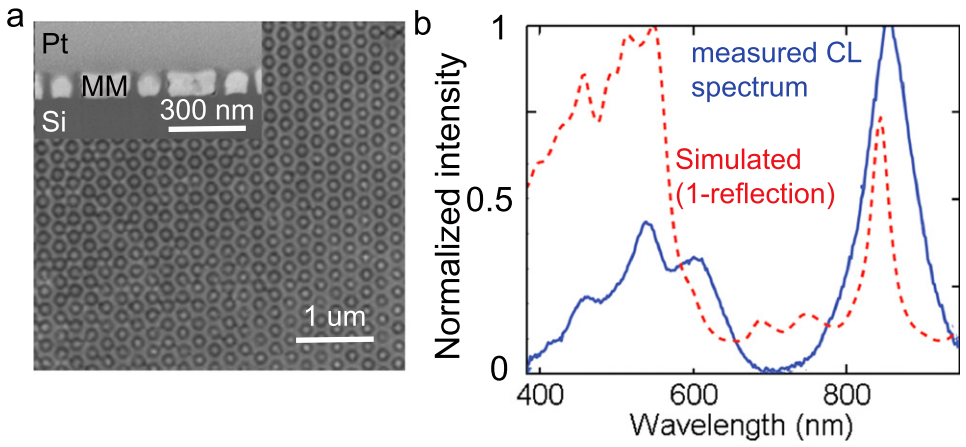

Figure 7. (a) SEM top view image of the 20 × 20 μm^2 Ag/Si coaxial array on a Si substrate used to measure the CL spectrum, where the dark rings represent the Si which is embedded in Ag. The rings have an outer diameter of 175 nm and a dielectric channel width of 30 nm. The pitch is 230 nm. The inset shows a SEM image of a cross section of the sample, where Pt was deposited in order to make a clean cross section. The measured CL spectrum is shown as the blue solid line in (b), corresponding to the normalized averaged spectrum over a single ring. The red dashed line shows the simulated one-reflection spectrum, for a 100 nm thick metamaterial on a $n = 4$ substrate and experimentally measured coax dimensions.

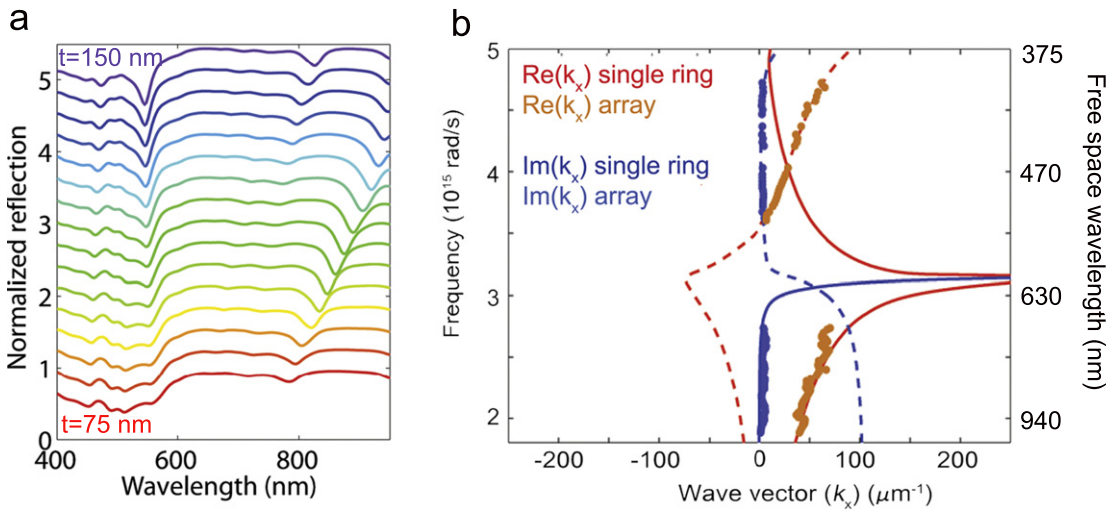

Figure 8. (a) Simulated reflection spectra for a coaxial metamaterial slab with rings with an outer diameter of 175 nm, a ring width of 30 and a 230 nm pitch for varying slab thicknesses from 75–150 nm. The spectra are offset for clarity. In (b) the dispersion diagram of a single, infinitely long coax (red and blue lines) is shown, where the real part is represented in red and the imaginary part in blue. The dashed lines are the negative-index mode, whereas the solid lines represent the positive-index mode. The data points on the dispersion diagram are the fitted wave vectors from FDTD simulations of a 5 μm thick metamaterial slab.

The metamaterial dimensions were as measured from the SEM image and we used values for the optical constants from Palik [38] for Si and Johnson and Christy [39] for Ag. Since the phase shift upon reflection depends on the refractive index of the supporting material, we included a dielectric slab with index 4 as substrate, approximating the Si substrate used in the experiment.

The simulated reflection results are shown in figure 8(a) where a dip in the reflection represents coupling of the incident source to a mode inside the metamaterial. We observe a dip at $\lambda \sim 800$ nm for the smallest thickness, which shifts to larger wavelengths for increasing slab thickness. This thickness dependence of the dip position indicates that the dip in reflection reflects coupling of light into a Fabry–Pérot resonance, a standing wave inside the material which is the result of interference with the incoupled light and waves reflected from both interfaces. Another indication that the peak at the red side of the spectrum represents a Fabry–Pérot oscillation is that the peak is absent in case the same simulations are performed without a substrate (not shown here). As in the case of the measured spectrum, we observe multiple features on the blue side of the spectrum in the simulated spectra shown in figure 8(a), in the range of $\lambda = 400$–600 nm. These features, however, do not

show a significant shift for a different slab thickness, which indicates that these dips are not Fabry–Pérot oscillations.

We observe that for a slab thickness of 100 nm the features of the simulated spectrum match those of the experimental spectrum best, as shown in figure 7(b). In the case of CL, the electron beam couples to the modes, of which the light scattered out of these modes is measured leading to intensity peaks in the spectrum. For the simulated reflection data, however, a dip in the spectrum represents light coupled to a mode. Therefore, we compare the simulated one-reflection data to the experimentally measured CL spectrum. We observe good agreement for both spectra in figure 7(b), in both peak position and spectral shape. However, the peak intensities are different, which can be explained by the different excitation mechanisms used in the experiment (electron beam) and simulations (plane wave).

The simulated and experimentally measured spectra can be further understood by considering the dispersion diagram, as shown in figure 8(b), where both the real and imaginary part of the mode dispersion is calculated for an infinitely long single coax. The dots in the figure represent dispersion data extracted from FDTD simulations of a coaxial array with the experimentally measured dimensions (except for the thickness, which was 5 μm for these simulations to avoid Fabry–Pérot oscillations). The wave vector is extracted by fitting a wave of the form $A\exp(ik_z z)$ to the simulated field inside the coaxes along the propagation direction. Here, A is the complex amplitude, k_z the wave vector in the propagation direction, and z the propagation distance along the z axis. From the good agreement we conclude that the dispersion of a single coax does coincide with that of a coaxial array. Due to the high losses in the region near the SP resonance frequency, no reliable fits could be made in this region. The fit can only be performed on the propagating mode in the system, which explains the jump from the positive to the negative mode for higher frequencies. This is in agreement with the mode with the lowest losses.

From figure 8 we find very high losses in the spectral range $\lambda = 600$–750 nm, which explains why the CL spectrum shows a dip in the signal at $\lambda = 700$ nm. From the dispersion diagram (calculated for azimuthal mode number 1) we find a mode index of $n \sim 7$ at $\lambda = 856$ nm, corresponding to a wavelength inside the material of 123 nm, close to the 100 nm thickness of the slab as assumed from the simulations of the Fabry $=$ Pérot resonance spectra. This difference can be due to the phase shift introduced at reflection and transmission at each interface. In the simulations this phase shift is inherently accounted for. This phase shift, however, is difficult to calculate due to the multimode nature of the system which is not accounted for in using for example the transfer matrix method [44]. Another explanation for the mismatch of the SPP wavelength and the slab thickness is a (small) error in the measured cylinder dimensions, as the mode index is especially sensitive to the width of the dielectric channels. The mode we observe here is very similar to a $n = 0, m = 1$ whispering gallery mode, where n is the number of field antinodes in the z-direction and m the azimuthal mode number, as reported earlier in literature for larger plasmonic rings [45, 46].

Next, we consider the smaller peaks at $\lambda = 461,\ 541,\ 603$ nm in the measurements shown in figure 7. The dispersion diagram in figure 8(b) shows that these peaks are in the highly dispersive regime of the spectrum, which makes it difficult to account for their nature. Since the peak positions do not shift with changing the thickness of the metamaterial (figure 8(a)), it suggests that these modes are not Fabry–Pérot resonances. However, it is difficult to prove this with certainty, due to the complicated dispersion behavior of the metamaterial. It also seems unlikely that these peaks represent coupling to surface modes in the lateral direction, which was verified by repeating the simulations with a pitch of 300 nm instead of 230 nm (not shown here). The results of these simulations show dips in the reflection spectrum at the same wavelengths as the simulations with a 230 nm pitch, indicating that the shorter-wavelength peaks are not sensitive to the coax spacing. The nature of these peaks in the spectra is subject for further research.

We note that the CL measurements are not polarization resolved. However, in earlier work we demonstrated that the optical response of the coaxial structures is polarization independent for normal-incident excitation [48], as is the case for CL. For off-normal incidence we numerically found that for large pitches (uncoupled coaxes) energy propagation is always along the waveguides. This implies that only the coupling efficiency into the SPP modes is dependent on the angle, not the mode index itself. These finding were for relatively small incident angles, up to 20° (where 0° is defined as normal incidence). In case of smaller pitches, where the coaxes do couple, we refer to the supplementary information of [37] where isotropic behavior is found for incident angles up to 50°.

4. Coupling of adjacent cylinders

Figure 8(b) already showed that the dispersion calculated for a single waveguide matches the dispersion extracted from FDTD simulations well for the considered metamaterial dimensions in this figure. This indicates that the coupling of adjacent waveguide channels is not sufficient to alter the mode index significantly. However,

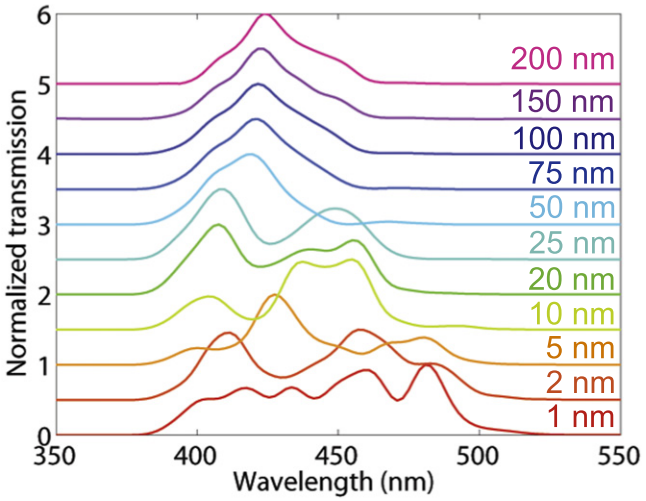

Figure 9. Transmission spectra of Si coaxes embedded in Ag, with an outer diameter of 168 nm and a dielectric channel width of 15 nm, where the ring-to-ring distance is systematically varied from 1 to 200 nm. The spectra were obtained from FDTD simulations, where a 200 nm thick free-standing metamaterial was illuminated by a plane wave under normal incidence.

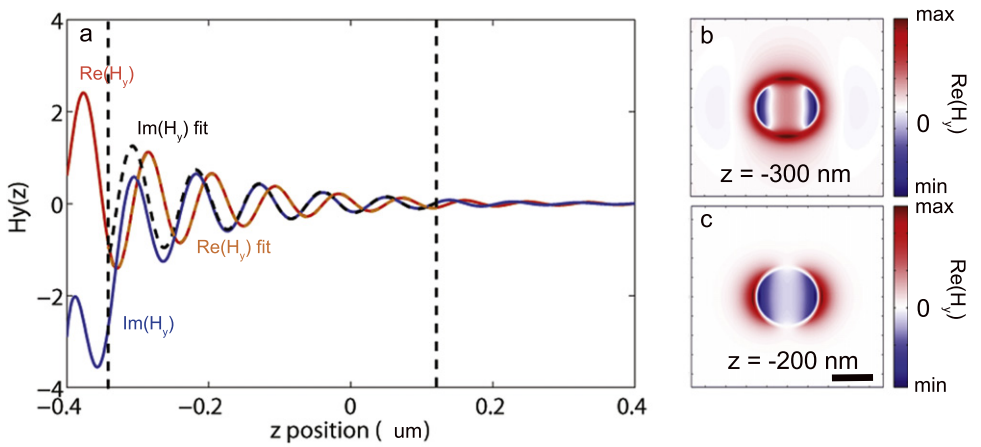

Figure 10. (a) Real (red) and imaginary (blue) H_y fields inside a Si waveguide channel in the propagation direction z, of coaxes with an outer diameter of 168 nm, a dielectric channel width of 15 nm and a ring-to-ring distance of 100 nm, embedded in Ag at $\lambda = 500$ nm. The interface of the metamaterial is positioned at $z = -400$ nm. The dashed orange and black lines represent the fits of the real and imaginary field respectively. The vertical black dashed lines indicate the region where the fit is performed, for smaller z-values multiple modes are present, and for larger propagation distances the field has decayed to very small values. (b) and (c) Show the H_y fields perpendicular to the propagation direction inside the waveguide channel at (b) $z = -300$ nm (100 nm from the metamaterial surface) and (c) -200 nm (200 nm from the metamaterial surface). The scale bar represents 100 nm.

when the coaxial channels are brought closer to each other, we expect to find a distance for which the modal fields of the adjacent channels start to overlap which will result in a change of the mode index. In this section, we explore at which ring-to-ring distances the coaxes start to couple by investigating coaxial arrays with different coax spacings.

Figure 9 shows the simulated transmission spectra for coaxial hexagonal arrays where the ring-to-ring distance is systematically varied from 1 to 200 nm. Here, the ring-to-ring distance is defined as the closest distance between the nearest neighbor. We simulated coaxes with an outer diameter of 168 nm and a dielectric channel width of 15 nm. We observe identical spectra for ring-to-ring distances of 75–200 nm. For closer spacings the spectrum clearly changes; new peaks arise over a broader spectral range.

This behavior is further investigated by considering the field profiles inside the metamaterial, along the waveguide channels. Figure 10(a) shows the H_y field intensities inside the waveguide channel along z, the propagation axis. For intermediate propagation distances (~150–500 nm from the metamaterial surface), an oscillating behavior is observed from which a single wavelength can be derived. At longer propagation distances (>500 nm) the field has decayed to very small intensities, and near the surface (<150 nm) we find a different behavior of the field as function of propagation distance. The latter observation is explained by multi-modal

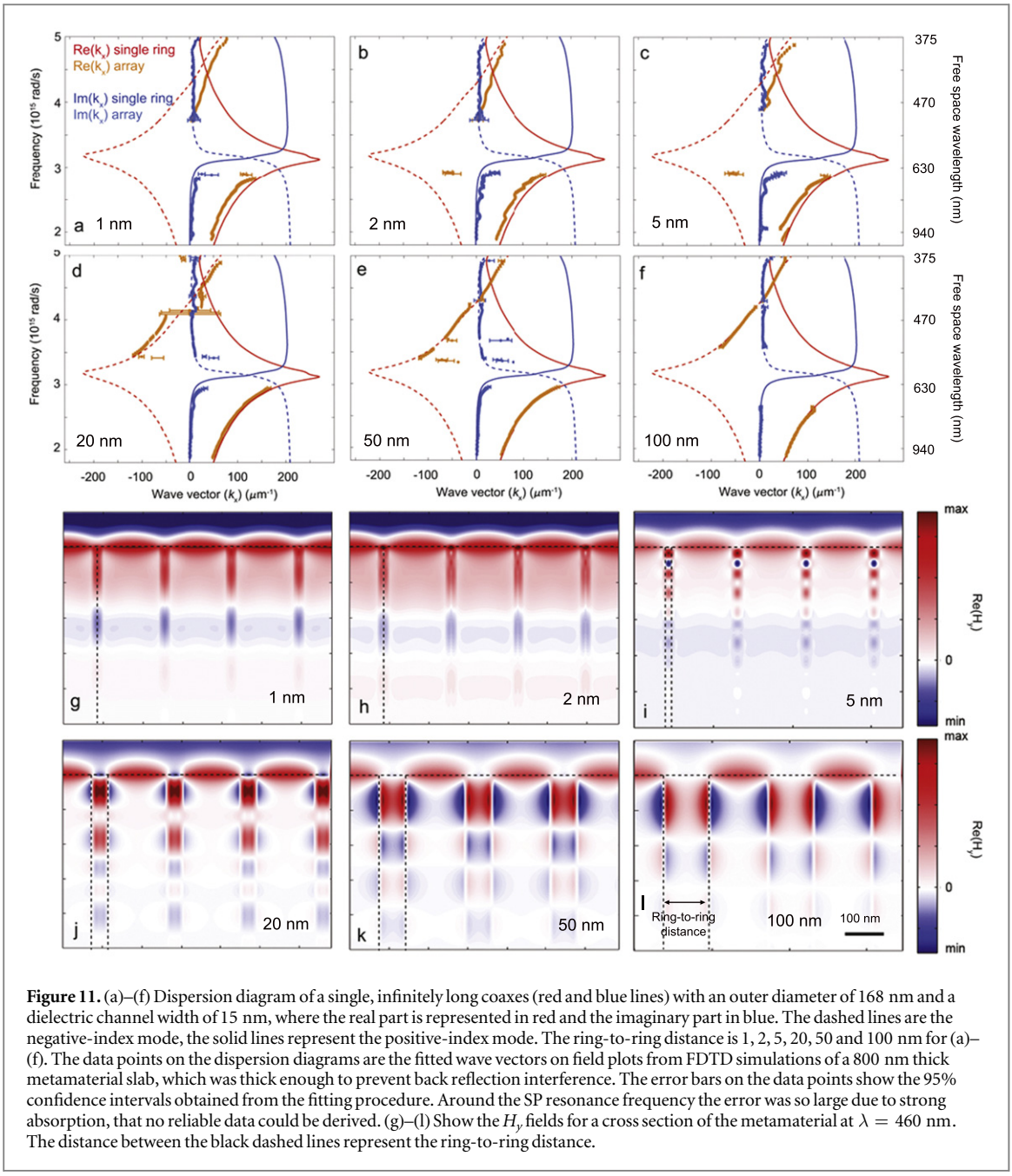

Figure 11. (a)–(f) Dispersion diagram of a single, infinitely long coaxes (red and blue lines) with an outer diameter of 168 nm and a dielectric channel width of 15 nm, where the real part is represented in red and the imaginary part in blue. The dashed lines are the negative-index mode, the solid lines represent the positive-index mode. The ring-to-ring distance is 1, 2, 5, 20, 50 and 100 nm for (a)–(f). The data points on the dispersion diagrams are the fitted wave vectors on field plots from FDTD simulations of a 800 nm thick metamaterial slab, which was thick enough to prevent back reflection interference. The error bars on the data points show the 95% confidence intervals obtained from the fitting procedure. Around the SP resonance frequency the error was so large due to strong absorption, that no reliable data could be derived. (g)–(l) Show the H_y fields for a cross section of the metamaterial at $\lambda = 460$ nm. The distance between the black dashed lines represent the ring-to-ring distance.

behavior, resulting in interference and thus alternated field profiles. Therefore, we obtain k_z by fitting the fields for z-values large enough that only the dominant mode was present, but small enough that the fields are not decayed to such small values that no accurate fit could be made. In figure 10(a) we show both the H_y intensity as function of propagation distance z and the fitted curves. We observe very good agreement between the simulated and fitted curves. Figures 10(b) and (c) show plots in the xy plane, perpendicular to the propagation direction, of Re(H_y) at different heights in the coax. The field profile in (b) is at 100 nm underneath the interface, showing a profile which is different than the expected field profile for the anti-symmetric mode as shown in figure 2. The plot in figure 10(c), however, shows the field profile of the propagating negative index mode. These results shows that indeed multiple modes compete with each other near the metamaterial surface, resulting in a field profile which is the result of interference of multiple modes, whereas after a certain distance only the propagating mode survives, resulting in the characteristic mode profile of only the anti-symmetric mode.

Figures 11(a)–(f) show the dispersion calculated for a single coax, together with the dispersion extracted from fits to the H_y field inside the waveguide channel of a coaxial array, as shown in (g)–(l) for ring-to-ring-distances of 1–100 nm. We find almost perfect agreement with the single coax case for 50 and 100 nm ring-to-ring distance. Decreasing the distance to 20 nm, however, does result in a small deviation of the dispersion diagrams as calculated for the single coax (d). Further decreasing the ring-to-ring distance leads to a more

distinct deviation from the single coax dispersion, where for the 1, 2 and 5 nm distance (a)–(c) the negative index mode has disappeared. This observation agrees well with the H_y mode profiles plotted in (g)–(l). At a ring-to-ring distance of 50 and 100 nm, we observe a typical mode profile of the anti-symmetric mode, where the field changes sign across the dielectric channel. At smaller ring-to-ring distances, however, we find that the field does not change sign across the channel.

Comparing the results observed from figure 11 with the simulated transmission spectra in figure 9, we conclude that there exists a range where we observe deviations in the transmission spectra, indicating coupling of the coaxes, but the dispersion is still similar to the single-coax dispersion. This is the case for ring-to-ring distances of 50–75 nm. For ring-to-ring distances of 20–50 nm we observe indications for coupling in both the transmission spectra and the dispersion diagrams, but in this region a negative index mode can still exist. These observations are important if the coaxial building-blocks are used to design a three-dimensional metamaterial, since this can only be achieved if the coaxes are coupled with each other.

5. Conclusions

We have investigated a coaxial plasmonic metamaterial consisting of dielectric rings embedded in metal. We show that the dispersion is very sensitive to the choice of material and geometry, and find that Si rings embedded in Ag with a diameter of 150–200 nm and a dielectric channel width of 10–30 nm have a negative-mode index with relatively low loss in the visible spectral range. We measure the optical modes of the metamaterial with CL spectroscopy on an experimentally fabricated coaxial array with a channel width and diameter of 30 and 175 nm, respectively. The measurements show that we are able to excite Fabry–Pérot resonances inside a 100 nm thick metamaterial slab. Furthermore, we numerically investigate the coupling behavior of adjacent coaxes inside a hexagonal array. We show that the transmission spectrum deviates from the spectrum of a single coax embedded in metal for ring-to-ring distances smaller than 50–75 nm, while the dispersion changes significantly for distances smaller than 20–50 nm. In very dense arrays (ring-to-ring distance <5 nm), we observe that the negative index mode can no longer exist. These findings are important for designing a metamaterial with a three-dimensional response.

Acknowledgments

This work is part of the research program of the Stichting voor Fundamenteel Onderzoek der Materie (FOM) which is part of the Nederlandse Organisatie voor Wetenschappelijk Onderzoek (NWO). It is also supported by NanoNextNL, a nanotechnology program funded by the Dutch Ministry of Economic Affairs, and the European Research Council (ERC). AP is co-founder and co-owner of Delmic BV, a startup company that has developed a commercial product based on the cathodoluminescence system that was used in this work.

References

[1] Veselago V G 1968 The electrodynamics of substances with simultaneously negative values of ϵ and μ *Sov. Phys. Usp.* **10** 509
[2] Shelby R A, Smith D R and Schultz S 2001 Experimental verification of a negative index of refraction *Science* **292** 77–9
[3] Valentine J, Zhang S, Zentgraf T, Ulin-Avila E, Genov D A, Bartal G and Zhang X 2008 Three-dimensional optical metamaterial with a negative refractive index *Nature* **455** 376–9
[4] Dolling G, Wegener M, Soukoulis C M and Linden S 2007 Negative-index metamaterial at 780 nm wavelength *Opt. Lett.* **32** 53–5
[5] Soukoulis C M, Linden S and Wegener M 2007 Negative refractive index at optical wavelengths *Science* **315** 47–9
[6] Rockstuhl C, Zentgraf T, Guo H, Liu N, Etrich C, Loa I, Syassen K, Kuhl J, Lederer F and Giessen H 2006 Resonances of split-ring resonator metamaterials in the near infrared *Appl. Phys.* B **84** 219–27
[7] Pines D 1956 Collective energy losses in solids *Rev. Mod. Phys.* **28** 184–98
[8] Ritchie R H 1957 Plasma losses by fast electrons in thin films *Phys. Rev.* **106** 874–81
[9] Hopfield J J 1958 Theory of the contribution of excitons to the complex dielectric constant of crystals *Phys. Rev.* **112** 1555–67
[10] Ritchie R H, Arakawa E T, Cowan J J and Hamm R N 1968 Surface-plasmon resonance effect in grating diffraction *Phys. Rev. Lett.* **21** 1530–3
[11] Kreibig U and Zacharias P 1970 Surface plasma resonances in small spherical silver and gold particles *Z. Phys.* **231** 128–43
[12] Cunningham S L, Maradudin A A and Wallis R F 1974 Effect of a charge layer on the surface-plasmon-polariton dispersion curve *Phys. Rev.* B **10** 3342–55
[13] Otto A 1968 Excitation of nonradiative surface plasma waves in silver by the method of frustrated total reflection *Z. Phys.* **216** 398–410
[14] Barnes W L, Dereux A and Ebbesen T W 2003 Surface plasmon subwavelength optics *Nature* **424** 824–30
[15] Dionne J A, Sweatlock L A, Atwater H A and Polman A 2005 Planar metal plasmon waveguides: frequency-dependent dispersion, propagation, localization, and loss beyond the free electron model *Phys. Rev.* B **72** 075405
[16] Economou E N 1969 Surface plasmons in thin films *Phys. Rev.* **182** 539–54
[17] Zia R, Selker M D, Catrysse P B and Brongersma M L 2004 Geometries and materials for subwavelength surface plasmon modes *J. Opt. Soc. Am.* A **21** 2442–6
[18] Dionne J A, Sweatlock L A, Atwater H A and Polman A 2006 Plasmon slot waveguides: towards chip-scale propagation with subwavelength-scale localization *Phys. Rev.* B **73** 035407

[19] Sainidou R and Garcia de Abajo F J 2008 Plasmon guided modes in nanoparticle metamaterials *Opt. Express* **16** 4499–506
[20] Verhagen E, de Waele R, Kuipers L and Polman A 2010 Three-dimensional negative index of refraction at optical frequencies by coupling plasmonic waveguides *Phys. Rev. Lett.* **105** 223901
[21] Maas R, Parsons J, Engheta N and Polman A 2013 Experimental realization of an epsilon-near-zero metamaterial at visible wavelengths *Nat. Photon.* **7** 907–12
[22] Moitra P, Yang Y, Anderson Z, Kravchenko I I, Briggs D P and Valentine J 2013 Realization of an all-dielectric zero-index optical metamaterial *Nat. Photon.* **7** 791–5
[23] Vesseur E J R, Coenen T, Caglayan H, Engheta N and Polman A 2013 Experimental verification of $n = 0$ structures for visible light *Phys. Rev. Lett.* **110** 013902
[24] Pendry J B 2000 Negative refraction makes a perfect lens *Phys. Rev. Lett.* **85** 3966–9
[25] Xu T, Agrawal A, Abashin M, Chau K J and Lezec H J 2013 All-angle negative refraction and active flat lensing of ultraviolet light *Nature* **497** 470–4
[26] Yu N and Capasso F 2014 Flat optics with designer metasurfaces *Nat. Mater.* **13** 139–50
[27] Engheta N 2007 Circuits with light at nanoscales: optical nanocircuits inspired by metamaterials *Science* **317** 1698–702
[28] Pendry J B, Luo Y and Zhao R 2015 Transforming the optical landscape *Science* **348** 521–4
[29] Pendry J B, Schurig D and Smith D R 2006 Controlling electromagnetic fields *Science* **312** 1780–2
[30] Edwards B, Alù A, Silveirinha M G and Engheta N 2009 Experimental verification of plasmonic cloaking at microwave frequencies with metamaterials *Phys. Rev. Lett.* **103** 153901
[31] Pendry J B, Aubry A, Smith D R and Maier S A 2012 Transformation optics and subwavelength control of light *Science* **337** 549–52
[32] Mhlig S, Cunningham A, Dintinger J, Farhat M, Hasan S B, Scharf T, Brgi T, Lederer F and Rockstuhl C 2013 A self-assembled three-dimensional cloak in the visible *Sci. Rep.* **3** 2328
[33] Landy N and Smith D R 2013 A full-parameter unidirectional metamaterial cloak for microwaves *Nat. Mater.* **12** 25–8
[34] Challener W A *et al* 2009 Heat-assisted magnetic recording by a near-field transducer with efficient optical energy transfer *Nat. Photon.* **3** 220–4
[35] Zia R, Schuller J A, Chandran A and Brongersma M L 2006 Plasmonics: the next chip-scale technology *Mater. Today* **9** 20–7
[36] de Waele R, Burgos S P, Atwater H A and Polman A 2010 Negative refractive index in coaxial plasmon waveguides *Opt. Express* **18** 12770–8
[37] Burgos S P, de Waele R, Polman A and Atwater H A 2010 A single-layer wide-angle negative-index metamaterial at visible frequencies *Nat. Mater.* **9** 407–12
[38] Palik E 1985 *Handbook of Optical Constants of Solids* (New York: Academic)
[39] Johnson P B and Christy R W 1972 Optical constants of the noble metals *Phys. Rev.* B **6** 4370–9
[40] Foteinopoulou S, Economou E N and Soukoulis C M 2003 Refraction in media with a negative refractive index *Phys. Rev. Lett.* **90** 107402
[41] Dionne J A, Verhagen E, Polman A and Atwater H A 2008 Are negative index materials achievable with surface plasmon waveguides? A case study of three plasmonic geometries *Opt. Express* **16** 19001–17
[42] García de Abajo F J 2010 Optical excitations in electron microscopy *Rev. Mod. Phys.* **82** 209–75
[43] Sapienza R, Coenen T, Renger J, Kuttge M, van Hulst N F and Polman A 2012 Deep-subwavelength imaging of the modal dispersion of light *Nat. Mater.* **11** 781–7
[44] Paul T, Menzel C, Śmigaj W, Rockstuhl C, Lalanne P and Lederer F 2011 Reflection and transmission of light at periodic layered metamaterial films *Phys. Rev.* B **84** 115142
[45] Vesseur E J R, García de Abajo F J and Polman A 2009 Modal decomposition of surface-plasmon whispering gallery resonators *Nano Lett.* **9** 3147–50
[46] Vesseur E J R, de Abajo F J G and Polman A 2010 Broadband purcell enhancement in plasmonic ring cavities *Phys. Rev.* B **82** 165419
[47] Silva A, Monticone F, Castaldi G, Galdi V, Alù A and Engheta N 2014 Performing mathematical operations with metamaterials *Science* **343** 160–3
[48] van de Haar M A, Maas R, Schokker H and Polman A 2014 Experimental realization of a polarization-independent ultraviolet/visible coaxial plasmonic metamaterial *Nano Lett.* **14** 6356–60